

See discussions, stats, and author profiles for this publication at: <https://www.researchgate.net/publication/260838306>

# Seeded Growth of Metal-Doped Plasmonic Oxide Heterodimer Nanocrystals and Their Chemical Transformation

ARTICLE in JOURNAL OF THE AMERICAN CHEMICAL SOCIETY · MARCH 2014

Impact Factor: 12.11 · DOI: 10.1021/ja500871j · Source: PubMed

CITATIONS

14

READS

104

7 AUTHORS, INCLUDING:



Xingchen Ye

University of California, Berkeley

57 PUBLICATIONS 2,757 CITATIONS

SEE PROFILE



Taejong Paik

University of Pennsylvania

25 PUBLICATIONS 570 CITATIONS

SEE PROFILE



Christopher B Murray

University of Pennsylvania

259 PUBLICATIONS 27,480 CITATIONS

SEE PROFILE

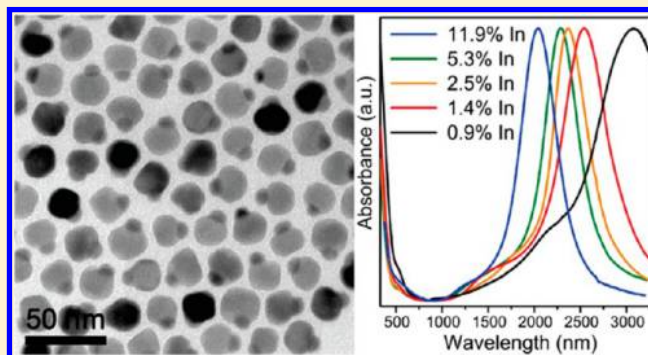
# Seeded Growth of Metal-Doped Plasmonic Oxide Heterodimer Nanocrystals and Their Chemical Transformation

Xingchen Ye,<sup>†</sup> Danielle Reifsnnyder Hickey,<sup>†</sup> Jiayang Fei,<sup>‡</sup> Benjamin T. Diroll,<sup>†</sup> Taejong Paik,<sup>†</sup> Jun Chen,<sup>†</sup> and Christopher B. Murray<sup>\*,†,‡</sup>

<sup>†</sup>Department of Chemistry and <sup>‡</sup>Department of Materials Science and Engineering, University of Pennsylvania, Philadelphia, Pennsylvania 19104, United States

## S Supporting Information

**ABSTRACT:** We have developed a generalized seeded-growth methodology for the synthesis of monodisperse metal-doped plasmonic oxide heterodimer nanocrystals (NCs) with a near-unity morphological yield. Using indium-doped cadmium oxide (ICO) as an example, we show that a wide variety of preformed metal NCs (Au, Pt, Pd, FePt, etc.) can serve as the seeds for the tailored synthesis of metal-ICO heterodimers with exquisite size, shape, and composition control, facilitated by the delayed nucleation mechanism of the CdO phase. The metal-ICO heterodimers exhibit broadly tunable near-infrared localized surface plasmon resonances, and dual plasmonic bands are observed for Au-ICO heterodimers. We further demonstrate that the oxide domain of the Au-ICO heterodimers can be selectively and controllably transformed into a series of partially and completely hollow cadmium chalcogenide nanoarchitectures with unprecedented structural complexity, leaving the metal domain intact. Our work not only represents an exciting addition to the rapidly expanding library of chemical reactions that produce colloidal hybrid NCs, but it also provides a general route for the bottom-up chemical design of multicomponent metal-oxide-semiconductor NCs in a rational and sequential manner.



## 1. INTRODUCTION

Colloidal heterodimer nanocrystals (NCs) are an emerging family of hybrid NCs comprised of distinct inorganic domains joined by well-defined metal–metal,<sup>1–8</sup> metal–semiconductor,<sup>9–17</sup> or metal–oxide<sup>18–25</sup> interfaces. This fascinating class of “artificial atoms” not only provides the possibility of combining dissimilar materials into a single multifunctional NC building block but also allows direct physical contact and therefore facilitates synergistic interactions and the charge and energy flow between the constituent NCs. Extensive studies have been performed over the past decade on developing synthetic strategies for heterodimer NCs, which hold great promise for applications including photocatalysis,<sup>26–29</sup> electrocatalysis,<sup>30</sup> bioimaging,<sup>17,31–33</sup> drug delivery,<sup>34</sup> sensing,<sup>35</sup> magnetism,<sup>36,37</sup> and electronics.<sup>38</sup>

Heterodimer NCs are typically synthesized by the heterogeneous nucleation of a secondary NC component onto the surface of a premade seed NC.<sup>7,19,20,39</sup> Recently a number of new reaction mechanisms have also been explored for the formation of heterodimer NCs, ranging from dealloying and phase segregation<sup>14,16,40,41</sup> to fusion of preformed NCs.<sup>9,20,42</sup> The synthesis of heterodimer NCs is inherently more complicated than that of monomeric NCs, and the fundamental processes of heterogeneous nucleation, particle growth, and ripening must still be better understood. Multiple reaction

pathways can often compete.<sup>5,9</sup> As a consequence, a judicious selection of reaction parameters is required to promote the formation of target heterodimers and to minimize the occurrence of homogeneous nucleation and the formation of other unfavorable side products. Despite the remarkable successes to date in designing heterodimer NCs with great compositional diversity, the synthesis of highly monodisperse heterodimer NCs with a near-unity morphological yield remains difficult, especially when a well-controlled doping profile of the subunit is also desirable.

In recent years, substantial research efforts have been devoted to the synthesis of degenerately doped semiconductors including chalcogenides,<sup>43–48</sup> nitrides,<sup>49</sup> and phosphides<sup>50</sup> as well as doped metal-oxide<sup>51–58</sup> NCs that exhibit localized surface plasmon resonance (LSPR) in the near-infrared (NIR) region. In contrast to conventional metallic plasmonic materials, such as Au and Ag, that exhibit a fixed carrier concentration, the carrier concentration and the LSPR frequency of these alternative plasmonic materials can be readily tuned by adjusting the doping level. To this end, a variety of chalcogenide and metal-oxide hosts have been identified to support tunable LSPR at NIR and mid-IR

Received: January 26, 2014

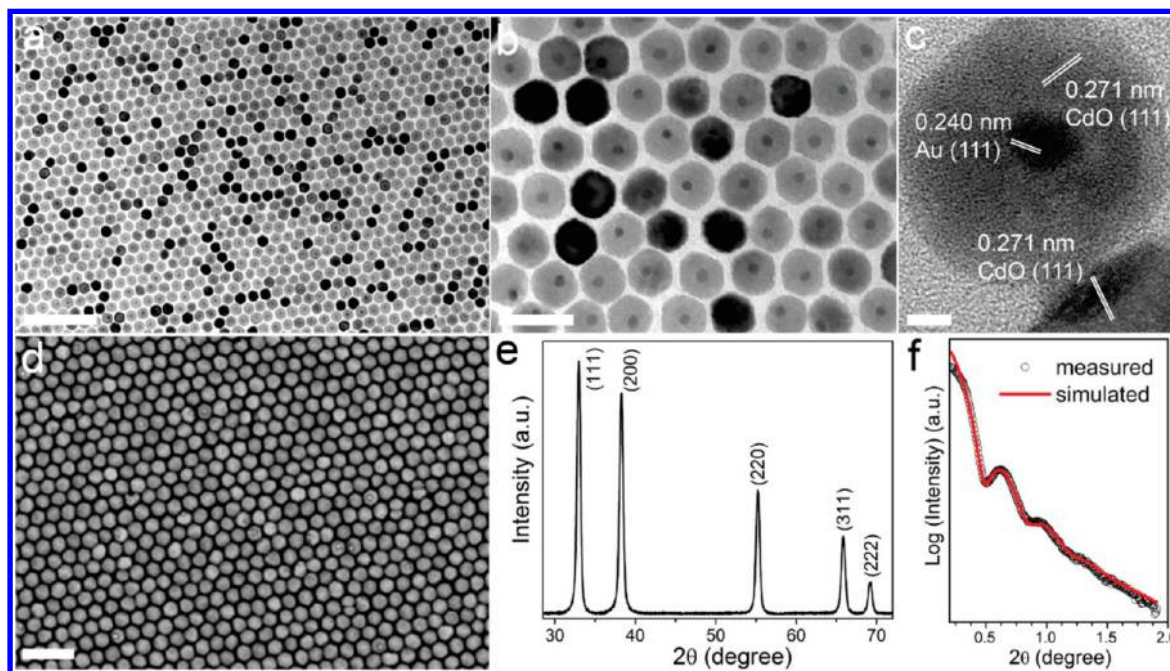


**Figure 1.** (a, b) TEM, (c) HRTEM, and (d) SEM images of 5.0 nm Au-ICO (5.3% In) heterodimer NCs and the corresponding (e) powder XRD and (f) SAXS patterns. Scale bars: (a) 200, (b) 50, (c) 5, and (d) 100 nm.

frequencies.<sup>43,44,47,49–54,56</sup> To harness the full potential of this new set of plasmonic building blocks, it is crucial to develop innovative strategies to incorporate them into colloidal hybrid NCs or higher-order clusters.

In the present work, we report, for the first time, the precision synthesis of monodisperse metal-doped plasmonic oxide heterodimer NCs. Using indium-doped cadmium oxide (ICO) as an example, we demonstrate that a rich array of metal-ICO heterodimer NCs can be synthesized by the nucleation of ICO NCs onto preformed metal-NC seeds. These metal-ICO heterodimers exhibit strong LSPR in the NIR range that is broadly tunable from 1.9 to 3.6  $\mu\text{m}$  by adjustment of the indium-doping level within the ICO NCs. Dual LSPR bands are observed for Au-ICO heterodimers, one in the visible range and the other in the NIR range. By exploiting the drastically different chemical reactivities of metals and oxides, we further demonstrate that the ICO domain of the heterodimers can be selectively transformed into a series of complex oxide/chalcogenide nanoarchitectures, leaving the metal NCs intact. Collectively, our work provides a general route for the bottom-up chemical design of multicomponent metal-oxide-chalcogenide NCs in a predictable and sequential manner.

## 2. RESULTS AND DISCUSSION

To synthesize metal-ICO heterodimer NCs, monodisperse metal-seed NCs (Au,<sup>59,60</sup> Pd,<sup>61</sup> Pt,<sup>62</sup> and FePt<sup>63</sup>) are first prepared according to literature methods and are introduced into the reaction mixture for ICO (Figure S1).<sup>56</sup> The thermal decomposition of the cadmium and the indium precursors at the reflux temperature ( $\sim 316^\circ\text{C}$ ) of the reaction solution induces the rapid nucleation of ICO onto the existing metal NCs. The transmission electron microscopy (TEM) images in Figure 1a,b show an example of highly uniform 5.0 nm Au-ICO heterodimers that readily self-assemble into ordered superlattices upon drop casting the NC dispersions onto a TEM grid. Au and ICO NCs with average diameters of  $5.0 \pm 0.3$  and 31.2

$\pm 1.8$  nm, respectively, are clearly discernible in the TEM images because of their difference in electron density. The high-resolution TEM (HRTEM) image in Figure 1c reveals that both the Au and the ICO domains are single crystalline. The lattice spacings for ICO and Au are measured to be 0.271 and 0.240 nm, respectively, which match well with the {111} lattice planes of both materials. Although one cannot exclude the possibility of a core-shell geometry based solely on the TEM results shown in Figure 1a,b, scanning electron microscopy (SEM) studies unambiguously confirm the heterodimer morphology (Figures 1d and S2). Notably, the SEM images reveal that the interfaces between the Au and the ICO domains are highly curved. In order to maintain a coherent interface, the ICO domain becomes concave during growth to accommodate the curvature of the existing Au-seed NCs (Figures 1d and S2), resulting in heterodimers with the smaller Au NCs partially embedded in the larger ICO NCs. Statistical analyses of TEM results reveal a morphological yield of  $\sim 98\%$  for heterodimers (estimated by counting a total number of 300 particles). The crystal phase and the size uniformity of the Au-ICO heterodimers are further studied using a combination of X-ray scattering techniques. The powder X-ray diffraction (XRD) pattern in Figure 1e shows intense peaks that correspond to the CdO phase.<sup>56,64</sup> Diffraction peaks from Au in the heterodimers are too weak to be detectable, which is reasonable given the small volume fraction of Au.<sup>14,19,20</sup> Small-angle X-ray scattering (SAXS) data can be fit by assuming ensembles of spherical particles with an average diameter of  $31.6 \pm 2.3$  nm (Figure 1f). The SAXS ringing patterns and the high quality of the fits validate that the samples are as uniform at the ensemble level as they appear under electron microscopy surveys (Figure 1f). Moreover, the size of the ICO domains of the heterodimers can be readily tailored from 22 to 40 nm by manipulating the oleic acid-to-cadmium molar ratio from 5.5 to 3.5 in the reaction solution (not shown), which is consistent with previous reports of ICO NCs alone.<sup>56,64</sup>



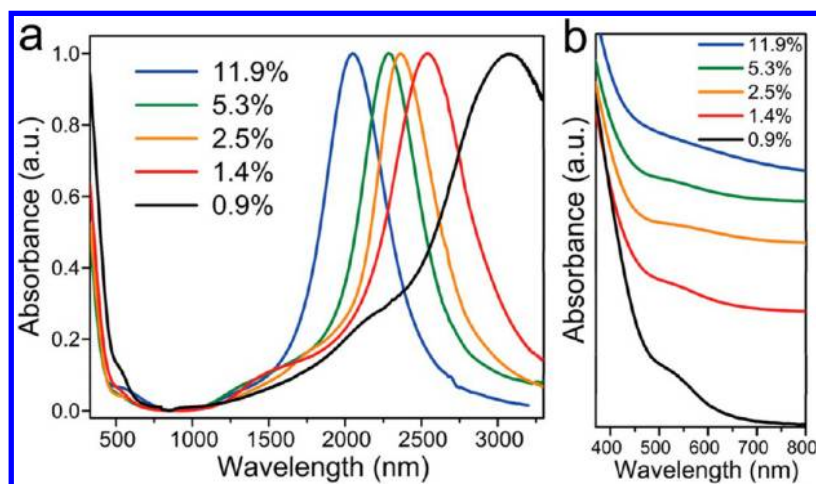


**Figure 2.** (a) UV-vis-NIR absorption spectra of 5.0 nm Au-ICO heterodimers dispersed in  $\text{CCl}_4$  as a function of the In-doping level. (b) Expanded shorter wavelength region of the spectra showing both the bandgap absorption from ICO and the plasmonic absorption from Au. The spectra are offset vertically for clarity.

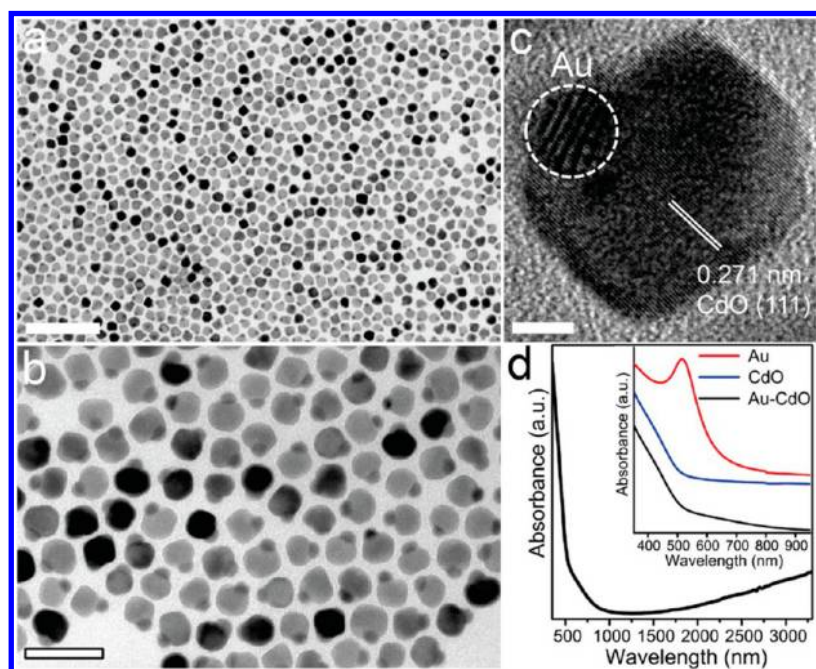


**Figure 3.** (a, b) TEM images, (c) HRTEM image and (d) UV-vis-NIR absorption spectrum of 5.0 nm Au-CdO heterodimers. The inset in (d) shows a comparison of the absorption spectra for pure 5.0 nm Au NCs, pure CdO NCs, and the 5.0 nm Au-CdO heterodimers. Scale bars: (a) 200, (b) 50, and (c) 5 nm.

Two distinct plasmon resonances arising from separate dipolar plasmon excitations in the Au and the ICO NCs are observed in the Au-ICO heterodimers (Figure 2a). The LSPR wavelength in the NIR range can be tuned from 1.9 to 3.6  $\mu\text{m}$  by adjusting the indium concentration of the ICO NCs. Furthermore, these Au-ICO heterodimers enable a direct comparison of the relative strength of the plasmonic resonances between the individual Au and ICO NCs. As depicted in Figure 2, the NIR LSPR band is substantially stronger and narrower than the visible one, indicative of a higher local electric field strength and a lower loss for the ICO NCs than for the Au NCs. From the perspective of the LSPR properties, these Au-ICO heterodimers can be regarded as the “optical equivalent” of very high aspect ratio ( $>10$ ) monodisperse gold nanorods, for which reliable syntheses remain a challenge.<sup>65,66</sup>

It has been well established that aliovalent cation doping in metal oxides can give rise to a higher charge carrier density and can therefore move the Fermi level above the conduction band minimum.<sup>52,56</sup> This effect, known as the Burstein–Moss shift,<sup>67</sup> is manifested by a blue shift of the absorption edge. Tauc plots ( $(\alpha h\nu)^2$  plotted against photon energy) of the UV-vis-NIR absorption data in Figure 2a show that, in general, as the indium concentration increases, the direct optical bandgap of the Au-ICO heterodimers widens (Figure S3).<sup>49,56</sup> However, an accurate determination of the bandgap remains difficult due to absorptions related to the LSPR and the interband transitions of Au NCs. Both of the LSPR energies of the Au-ICO heterodimers decrease with increasing refractive index of the solvent, consistent with what one would expect for an LSPR feature (Figure S4).<sup>45</sup>

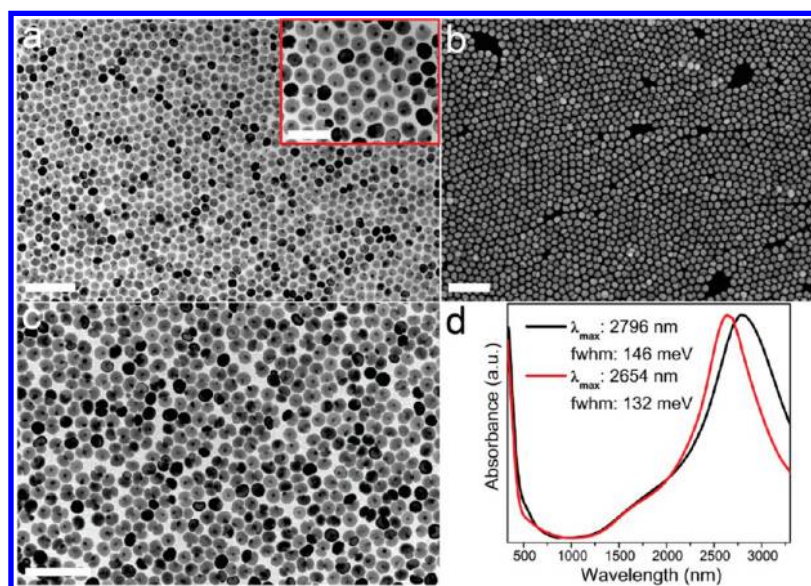


**Figure 4.** (a) TEM and (b) SEM images of 9.4 nm Au-ICO (0.9% In) heterodimers. (c) Representative TEM image of Au-ICO heterostructures (1.0% In) synthesized using half the amount of Au NC seeds as those used for the samples shown in (a) and (b). Scale bars: (a) 200, (a, inset) 100, (b) 200, and (c) 200 nm. (d) UV-vis-NIR absorption spectra for the samples shown in (a, b) (black curve) and (c) (red curve).

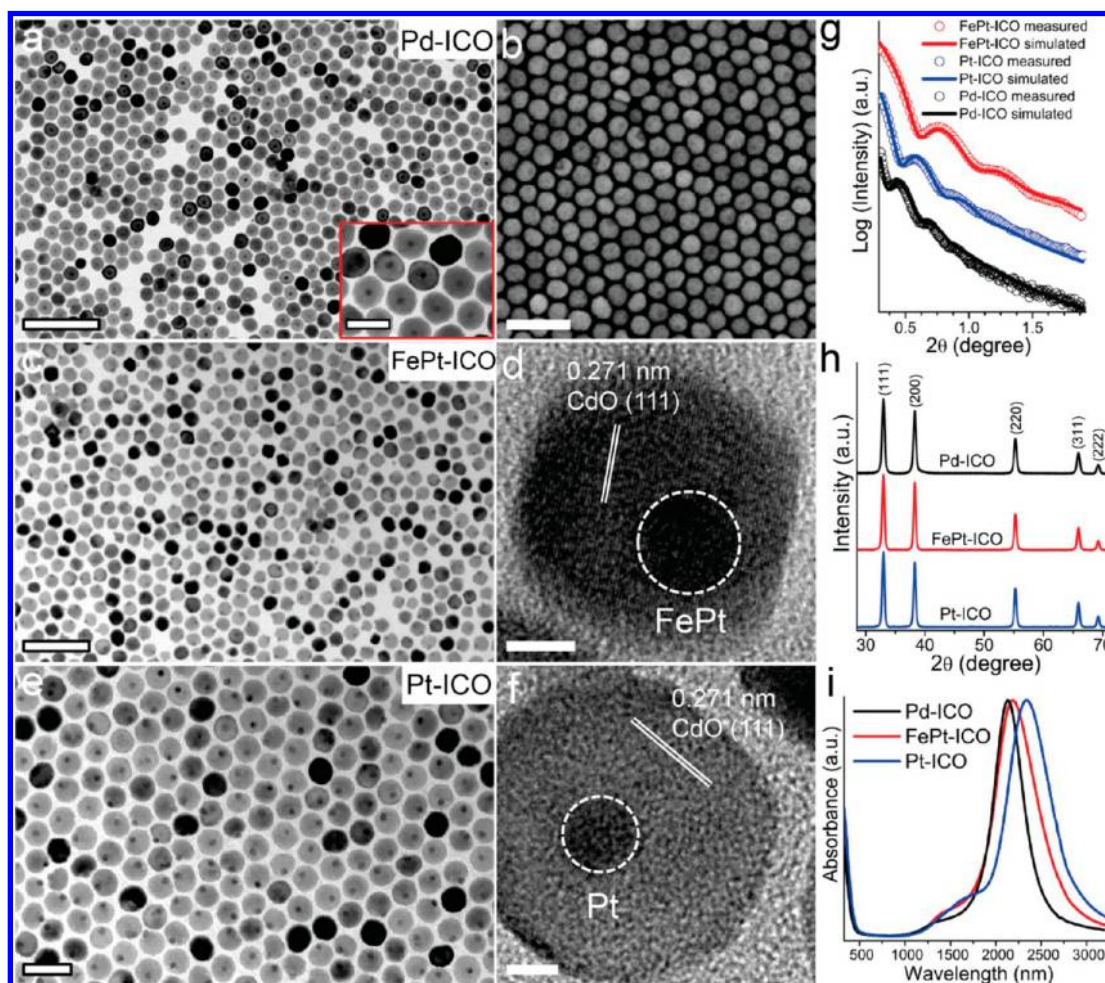


**Figure 5.** (a) TEM and (b) SEM images of Pd-ICO (6.5% In) heterodimers. (c) TEM and (d) HRTEM images of FePt-ICO (6.1% In) heterodimers. (e) TEM and (f) HRTEM images of Pt-ICO (3.4% In) heterodimers. Scale bars: (a) 200, (a, inset) 50, (b) 100, (c) 100, (d) 5, (e) 50, and (f) 5 nm. (g, h) Experimental and simulated SAXS (g) and powder XRD patterns (h). (i) UV-vis-NIR absorption spectra for Pd-ICO, FePt-ICO, and Pt-ICO heterodimers.



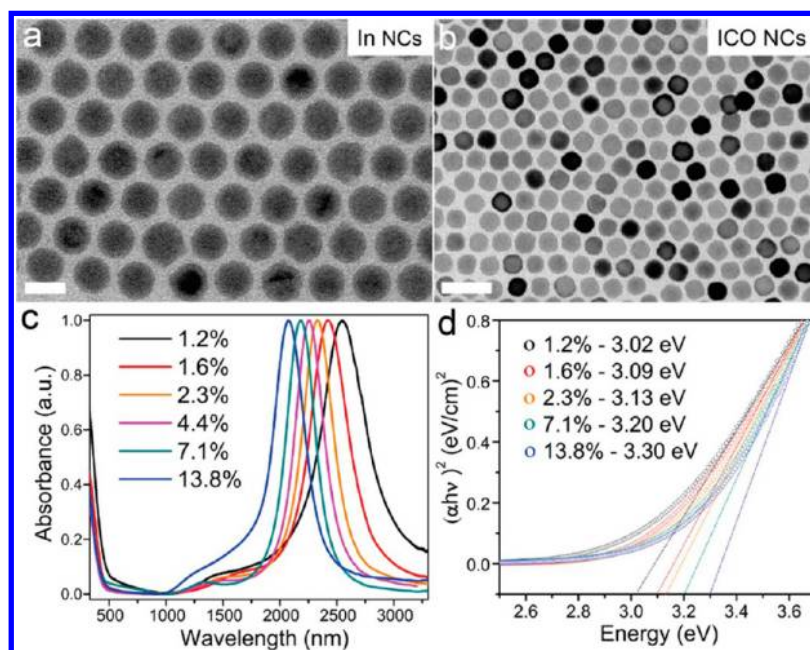


**Figure 6.** TEM images of (a) 14.8 nm In and (b) ICO NCs and (c, d) optical evidence for the conversion of In NCs into doped ICO NCs. Essentially, the In NCs dissolve during the heat-up process and function as the In precursor for doping of the CdO lattice. Scale bars: (a) 20 and (b) 50 nm. (c) Absorption spectra of ICO NCs with increasing In doping (resulting from increased concentrations of In NCs). (d) Plots of  $(\alpha h\nu)^2$  vs photon energy (eV) with linear fits (dotted lines) to extract the direct bandgap energies.

Monodisperse 5.0 nm Au-CdO heterodimers can also be synthesized when the indium precursor is absent (Figure 3a,b). HRTEM imaging reveals that both NC domains of the heterodimers are single-crystalline (Figure 3c). Distinct moiré fringes, which appear as dark bands in the Au-CdO interface region with a periodicity of  $\sim 0.87$  nm, are due to the interference between the diffracted electron beams from the overlapping Au (111) and CdO (111) lattice planes with a rotation angle of  $14.7^\circ$ .<sup>68</sup> The UV-vis-NIR spectrum for the Au-CdO heterodimers shows no distinct peak; instead, the absorption increases slightly in the NIR region, which is likely caused by the presence of intrinsic defects, such as oxygen vacancies and interstitial Cd atoms within the CdO lattice, both of which can generate free carriers (Figure 3d).<sup>69</sup> In comparison to pure CdO NCs, Au-CdO heterodimers show increased absorption in the visible region due to the presence of Au, yet the visible LSPR band red-shifts and broadens relative to that of pure Au NCs (Figure 3d, inset).

We also examine the effects of the Au NC size on the heterodimer formation. As shown in Figure 4a,b, when an optimal amount of 9.4 nm oleylamine-capped Au NCs are used as the seeds, predominantly Au-ICO heterodimers and a small fraction ( $\sim 5\%$ ) of ICO-Au-ICO heterotrimers are obtained. A further decrease in the concentration of the Au seeds leads to an increased population of heterotrimers (70%),<sup>20,42</sup> with the remainder consisting of heterodimers (10%) and petal-like structures ( $\sim 20\%$ ), in which multiple ICO domains grow off a single Au NC (Figure 4c). This observation contrasts with the above case of 5.0 nm Au seeds, where reducing the concentration of Au seeds yields a mixture of isolated ICO NCs and Au-ICO heterodimers rather than a predominance of heterotrimers (not shown). Therefore, it appears that increasing the size of the Au seeds from 5.0 to 9.4 nm increases the available surface area of Au and, thus, reduces the steric hindrance for the nucleation and growth of multiple ICO domains.<sup>70</sup> Optical absorption spectra show that the visible

LSPR band for the sample presented in Figure 4c is red-shifted relative to that of the heterodimers shown in Figure 4a,b, which is attributed to a higher refractive index surrounding the individual Au NCs, due to their close proximity to a greater number of ICO NCs (Figure 4d). In contrast, the NIR LSPR band does not follow the same trend but correlates with the actual indium-doping level of the final samples, measured by ICP-OES.

We further explore the generality of this seeded growth method for other metal-ICO heterodimer NCs. As shown in Figure 5, monodisperse Pd-ICO (Figure 5a,b), FePt-ICO (Figure 5c,d), and Pt-ICO (Figure 5e,f) heterodimers can be synthesized when the corresponding metal or metal-alloy NCs are used as seeds. Figure 5g presents experimental SAXS patterns acquired from concentrated toluene solutions of various heterodimers. The SAXS patterns are simulated from polydisperse ensembles of spherical particles with average diameters of  $41.4 \pm 3.9$  nm (for the Pd-ICO dimer),  $31.6 \pm 2.8$  nm (for the Pt-ICO dimer), and  $24.0 \pm 2.1$  nm (for the FePt-ICO dimer), which are in excellent agreement with the sizes of the nearly spherical ICO domains measured from the TEM images. The powder XRD patterns of the three types of heterodimers exhibit characteristic peaks that can be readily assigned to the CdO phase, whereas diffraction peaks from the metal NCs are not observable, which is analogous to the case of Au-ICO heterodimers (Figure 5h). A sharp LSPR peak is also present in the NIR frequencies for these metal-ICO heterodimers, and a significantly reduced absorption in the visible range (450 to 700 nm) is observed compared to that of the Au-ICO heterodimers because of the nonplasmonic character of the Pd, Pt, and FePt NCs (Figure 5i).

The chemical versatility of the metal-ICO heterodimer can be attributed to the following reasons. First, the formation of CdO follows a unique “delayed nucleation” pathway.<sup>71</sup> Specifically, CdO NCs do not form when the reaction mixture first reaches the reflux temperature ( $\sim 316^\circ\text{C}$ ). Instead, for the

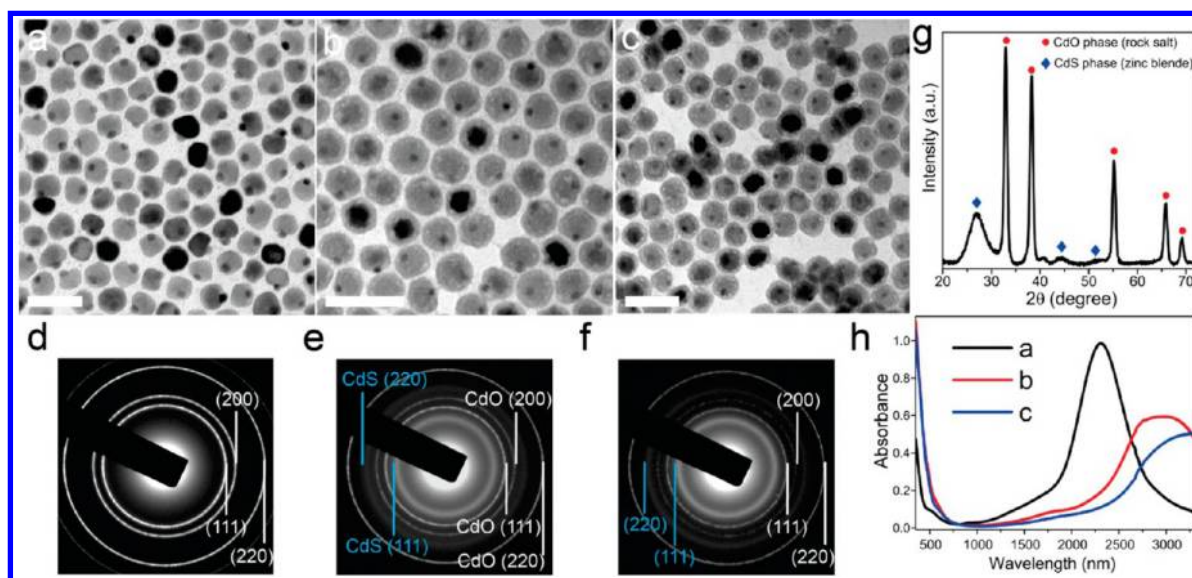


**Figure 7.** (a–c) TEM images and (d–f) corresponding SAED patterns of pristine Au-ICO (5.6% In) heterodimers (a, d) and Au-ICO@CdS heterodimers synthesized by reacting Au-ICO heterodimers with  $(\text{NH}_4)_2\text{S}$  at a Cd:S molar ratio of 2:1 (b, e) and 1:1 (c, f), respectively. All scale bars represent 50 nm. The SAED patterns were acquired from a sample area of  $\sim 60 \mu\text{m}^2$ . (g) Powder XRD patterns of the Au-ICO@CdS heterodimers shown in (b). (h) UV–vis–NIR spectra of the samples shown in (a–c). The spectra have been vertically offset slightly to have an identical absorbance value at 800 nm.

typical oleic-acid-to-metal molar ratio of 5:1 used in this work, the nucleation of CdO occurs very rapidly after refluxing for an extended period of time (40–50 min), as evidenced by a rapid color change of the reaction mixture from transparent to whitish-gray (indicating the formation of metallic Cd NCs), followed by another rapid color change to brownish (indicating the nucleation of the CdO phase) within a few seconds. This induction period can be explained in the context of the equilibrium between the thermally induced metal–oxygen bond breaking of the cadmium (and indium) precursors for the accumulation of the active species for nucleation and the complexation of cadmium carboxylate precursors with oleic acid to form cadmium oleate *in situ*.<sup>72</sup> This argument is supported by the observation that increasing the oleic acid concentration in the reaction mixture leads to a longer induction period. Powder XRD patterns of a series of aliquots withdrawn from the reaction solution immediately after the initial color change to the brownish color indicate that hexagonal-phase Cd metal NCs are formed at the beginning of nucleation, the fraction of which gradually diminishes during prolonged heating as a small quantity (<5% of Cd in the starting precursor based upon ICP-OES analyses) of large Cd NCs (>300 nm) precipitate out of the reaction solution (Figure S5).<sup>72</sup> Ultimately, the formation of heterodimers rather than that of a core–shell geometry is favored by the delayed burst nucleation of the CdO phase. Second, as shown in Figure S7, a physical mixture of seed and ICO NCs is obtained when  $\text{UO}_2$  or  $\text{Fe}_3\text{O}_4$  NCs are used as the seeds, suggesting that alloying between cadmium and certain metallic species at the metal–oxide interface of the heterodimers could play advantageous roles in dictating the formation of heterodimers.

Low-melting-point metal NCs such as indium are also employed as seeds (Figure 6a). Experimentally, before the reaction solution reaches the reflux temperature ( $\sim 316^\circ\text{C}$ ), In NCs are already completely dissolved into the mixture. However, we find that the dissolved indium species serve as the precursor for doping into the CdO lattice, and as a

consequence, highly monodisperse ICO NCs are formed (Figure 6b). The doping level can be easily adjusted by varying the amount of added In NCs, which gives rise to a narrow LSPR band tunable from 1950 to 3300 nm in the NIR range (Figure 6c). It is important to note that the quality factor for these ICO NCs, defined as the ratio of the LSPR energy to the plasmon line width, falls in the range of 5.2–7.5 (Table S1), which is far superior to that of other previously identified semiconductor-based plasmonic NCs.<sup>45,47,49,52,54</sup>

Chemical transformation of existing inorganic nanostructures has emerged as a versatile approach for the synthesis of unconventional hybrid NCs with programmable structural, morphological, and compositional complexity.<sup>73–83</sup> We further study the formation of metal–semiconductor heterostructures through the regioselective transformation of metal-doped oxide heterodimer NCs. Ammonium sulfide ( $(\text{NH}_4)_2\text{S}$ ) is used as the source of  $\text{S}^{2-}$  ions to selectively convert the oxide domain of the heterodimer into a sulfide material through an anion exchange process.<sup>80,82,84</sup> Because of its ionic character,  $(\text{NH}_4)_2\text{S}$  can readily provide  $\text{S}^{2-}$  species under modest reaction conditions, making it highly reactive toward a variety of metal complexes.<sup>84,85</sup> In a typical reaction, anhydrous  $(\text{NH}_4)_2\text{S}$  dissolved in oleylamine is injected into a reaction mixture containing heterodimer NCs, oleylamine, and 1-octadecene, and the reaction is allowed to proceed at  $70^\circ\text{C}$  for 5 min, as described in greater detail in the Supporting Information. Figure 7 shows a series of products from reacting Au-ICO heterodimers with increasing concentrations of  $(\text{NH}_4)_2\text{S}$ . From the TEM images shown in Figure 7a–c, it can be seen that the original heterodimer morphology is retained upon reaction with small amounts of  $(\text{NH}_4)_2\text{S}$ . Meanwhile, pinholes begin to develop within the outer surface layers of the ICO NCs, which leads to a distinct shell, as indicated by the brightness contrast in the TEM images. The structural evolution is also manifested in the corresponding SAED patterns (Figure 7d–f). Figure 7d shows only the CdO diffraction rings for the pristine Au-ICO heterodimers, whereas Figure 7e,f shows a progressive decrease



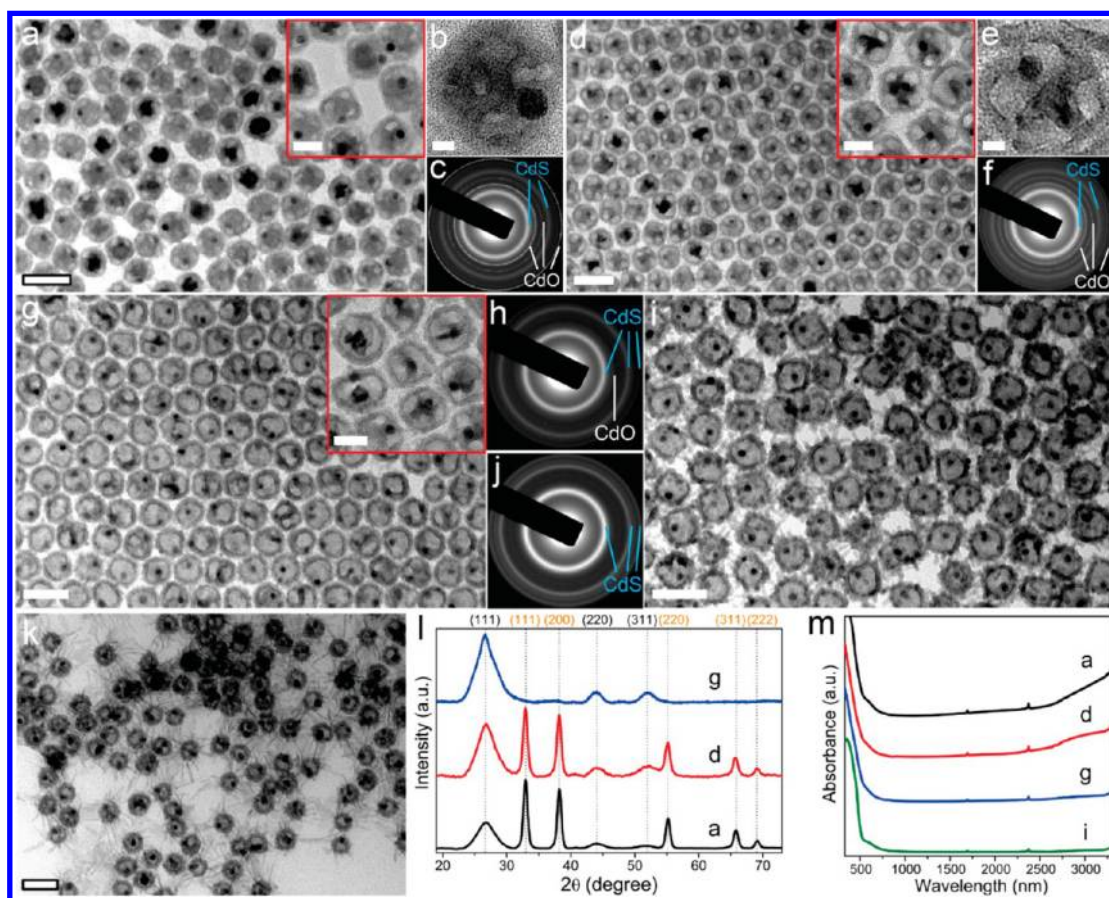


**Figure 8.** (a–k) TEM and HRTEM images and corresponding SAED patterns of samples synthesized by reacting Au-ICO (5.6% In) heterodimers with  $(\text{NH}_4)_2\text{S}$  at a Cd:S molar ratio of 1:2 (a–c), 1:3 (d–f), 1:4 (g,h), 1:6 (i,j), and 1:7.5 (k), respectively. The SAED patterns were acquired from a sample area of  $\sim 60 \mu\text{m}^2$ . Scale bars: (a) 50, (a, inset) 20, (b) 5, (d) 50, (d, inset) 20, (e) 5, (g) 50, (a, inset) 20, (i) 50, and (k) 50 nm. (l) Powder XRD patterns of the samples shown in (a), (d) and (g). (m) UV–vis–NIR spectra of the samples shown in (a), (d), (g), and (i).

in the intensity of the CdO diffraction rings and the appearance of increasingly intense zinc-blende CdS peaks. The powder XRD pattern proves the coexistence of the two phases, rock-salt CdO and zinc-blende CdS (Figure 7g). Our results are in stark contrast to the results of a previous study of the transformation of CoO into hollow cobalt sulfide NCs, where a postexchange high-temperature ( $>180^\circ\text{C}$ ) annealing step is necessary to convert the amorphous  $\text{CoS}_x$  into a crystalline shell.<sup>84</sup> Figure 7h displays the optical absorption data for the samples shown in Figure 7a–c. A weakening and a red shift of the ICO LSPR are observed for the samples shown in Figure 7b,c, which can be accounted for by a reduced indium-doping level (2.7% and 2.1% In, respectively, measured by ICP-OES), along with the formation of a sulfide shell that increases the average dielectric constant surrounding the ICO NCs. Furthermore, there is an increase in the absorption intensity below 500 nm, which is consistent with the bandgap absorption of nanocrystalline CdS. The Au LSPR peak is red-shifted and broadened due to plasmon dephasing at the metal–semiconductor interface (Figure 7h).<sup>86</sup>

When a larger amount of  $(\text{NH}_4)_2\text{S}$  is introduced at the beginning of the reaction, the ICO domain of the heterodimers becomes increasingly hollow, resulting in a cage-like structure with a porous shell (Figures 8a,d and S8a–d).<sup>10,79,80</sup> Both the CdS and the CdO phases are clearly visible in the corresponding SAED (Figure 8c,f) and XRD patterns (Figure 8i). The HRTEM images reveal no obvious change to the Au

region but show uneven contrast in the remaining ICO region, which suggests the coexistence of both CdO and CdS grains. It is observed that, in these partially exchanged NCs, there are inorganic bridges that connect the inner ICO core with the outer CdS shell (Figure 8a,b,d,e,g), providing ion transport channels that can drive the oxide-to-sulfide conversion toward completion when a sufficient quantity of  $\text{S}^{2-}$  ions is present.<sup>80</sup> The expansion of voids inside the individual ICO NCs can be interpreted based upon the faster outward diffusion of the core  $\text{Cd}^{2+}$  and  $\text{O}^{2-}$  ions than the incoming  $\text{S}^{2-}$  ions.<sup>79,80,84</sup> The unbalanced diffusion rates of the different ions help localize the reaction front at the outermost surface of the ICO NCs, yielding a hollow geometry as a result of nanoscale Kirkendall effects.<sup>79,80,87</sup> Small CdS NCs nucleate at multiple sites on the ICO surface as the conversion of ICO to CdS proceeds. A complete transformation from ICO to CdS is observed when the S:Cd ratio is greater than 4:1 (Figures 8g,i,k and S8e–h). At sufficiently high concentrations of  $\text{S}^{2-}$  ions, hollow CdS NCs with attached rod-like CdS branches are obtained (Figure 8i,k). It is noteworthy that the extent of side nucleation of CdS NCs in the bulk solution during the anion exchange process is usually negligible, which differs substantially from the oxide-to-selenide conversion, as discussed below. The morphological evolution illustrated in Figure 8 is also corroborated by the optical absorption data (Figure 8m). It is evident that sub-500 nm CdS absorption becomes dominant in the spectrum, with a concomitant loss of intensity from the NIR LSPR absorption.



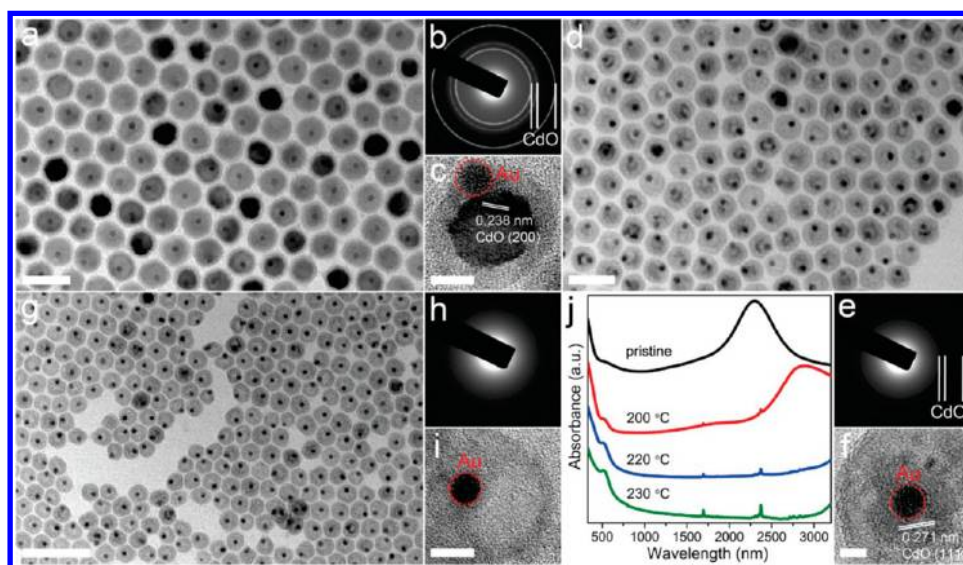


**Figure 9.** (a–i) TEM images, SAED patterns, and HRTEM images of samples synthesized by reacting Au-ICO (5.3% In) heterodimers with TBP-Se at different temperatures: (a–c) 200 °C; (d–f) 220 °C, and (g–i) 230 °C. The SAED patterns were acquired from a sample area of  $\sim 60 \mu\text{m}^2$ . Scale bars: (a) 50, (c) 10, (d) 50, (f) 5, (g) 100, and (i) 5 nm. (j) UV–vis–NIR spectra of the pristine Au-ICO heterodimers and the samples shown in (a–c).

Figure 9 presents the experimental results from the reaction of the Au-ICO heterodimers with the tributylphosphine-selenium (TBP-Se) complex. Here, a fixed Cd:Se ratio of 1:40 is used, and the reaction temperature is varied from 200 to 230 °C. At 200 °C, the size of the ICO region shrinks, forming a core-shell structure consisting of an ICO core with an amorphous, low-contrast shell, perhaps having a composition of  $\text{CdO}_x\text{Se}_{1-x}$  (Figure 9a–c). At 220 °C, the ICO region shrinks further, becoming less pronounced in both the HRTEM image and the SAED pattern (Figure 9d–f). At 230 °C, the ICO core has disappeared, both in the TEM image, which shows evidence of only a low-contrast shell, and in the SAED pattern, in which the CdO diffraction rings are no longer present (Figure 9g–i). It is clear that, after reacting with TBP-Se at 220 or 230 °C, the Au domain of the Au-ICO heterodimers persists, and the partially converted intermediates still exist with the nearly spherical shape of the original heterodimers. The disappearance of ICO is also supported by the absorption spectra shown in Figure 9j. The pronounced NIR plasmonic peak in the pristine Au-ICO heterodimer red-shifts and decreases considerably in intensity upon reaction with TBP-Se. At each reaction temperature (200, 220, and 230 °C), a peak appears in the visible region at  $\sim 520 \text{ nm}$ , in accordance with both the Au LSPR absorption and the position of the band edge absorption of quantum-confined CdSe NCs. The TEM images in Figure 9, which have been confirmed to be representative of the samples by imaging many regions on each TEM grid, show little evidence of small CdSe NCs as side products. However, it is important to point out that, unlike the anion exchange reaction with  $(\text{NH}_4)_2\text{S}$  as mentioned above, the reaction of Au-ICO heterodimers with TBP-Se does yield an appreciable quantity of small CdSe NCs in the bulk solution. The samples shown in Figure 9 have undergone size-selective precipitation to remove the small CdSe NCs, the amount of which increases monotonically with a higher reaction temperature. Consequently, it is possible that a small number of these CdSe NCs still remain in the sample and contribute to the absorption spectra shown in Figure 9j. As a control experiment, the same set of reactions is performed using pure ICO NCs instead of

Au-ICO heterodimers under otherwise identical conditions, and a similar temperature-dependent conversion behavior is observed (Figure S10). A further increase of the reaction temperature to 240 °C leads to well-defined hollow interiors within the initial ICO domains, and a corresponding higher fraction of small CdSe NCs that can still be isolated from the hollow heterostructures (Figure S11). At 280 °C, the initial ICO domains are completely digested, and high-quality zinc-blende (cubic) CdSe NCs are obtained, along with residual Au NCs originating from the Au-ICO heterodimers (Figure S12).

### 3. CONCLUSIONS

In summary, we have developed a generalized seeded-growth methodology for the high-yield synthesis of monodisperse metal-doped plasmonic oxide heterodimer NCs. Using indium-doped cadmium oxide as an example for the plasmonic oxide, we demonstrate that a wide variety of premade metal and metal-alloy NCs, including Au, Pt, Pd, and FePt NCs, can serve as the seeds for the tailored synthesis of metal-ICO heterodimers with exquisite size, shape, and composition control, facilitated by the delayed nucleation mechanism of the CdO phase. The resultant multicomponent NCs retain their individual LSPR properties, which are dependent on the choice of the seed NCs for the metallic domain and on the indium-doping level of the oxide domain. We further demonstrate that the oxide domain of the heterodimers can be selectively and controllably transformed into partially or completely hollow cadmium chalcogenide nanoshells by an anion exchange reaction with  $(\text{NH}_4)_2\text{S}$  or reaction with a phosphine-selenium complex, accompanied by nanoscale Kirkendall effects. A series of metal-oxide-chalcogenide and metal-chalcogenide hybrid nanoarchitectures can be accessed, including yolk-shell NCs with hollow interiors and porous shells, open cage-like nanostructures, and hollow NCs with continuous shells, most of which are not otherwise accessible through conventional synthetic methods. Altogether, our work opens up a new avenue for the chemical design of optically active heterostructured NC building blocks for applications

including plasmonic sensing, bioimaging, light harvesting, and photocatalysis. The seeded growth of metal-doped oxide heterodimer NCs represents an exciting addition to the rapidly expanding library of prototype chemical reactions that produce colloidal hybrid NCs. Given the size uniformity and the inherent chemical anisotropy presented by these heterodimers, further developments in site-selective chemical modification and directed self-assembly into predictive hierarchical structures can be anticipated.

## ■ ASSOCIATED CONTENT

### Supporting Information

TEM images of the various metal NCs; additional SEM images and Tauc plots for the 5.0 nm Au-ICO heterodimers with various In-doping levels; absorption spectra of Au-ICO heterodimers dispersed in three different solvents; powder XRD patterns of aliquots withdrawn from the Au-ICO heterodimer reaction after the initial color change; TEM images of the products synthesized by using  $\text{UO}_2$ ,  $\text{Fe}_3\text{O}_4$ , and Cu NCs as the seeds; additional TEM, SEM, and HRTEM images for the samples shown in Figures 8 and 9; and results from reacting Au-ICO heterodimers with TBP-Se at 240 and 280 °C. This material is available free of charge via the Internet at <http://pubs.acs.org>.

## ■ AUTHOR INFORMATION

### Corresponding Author

[cbmurray@sas.upenn.edu](mailto:cbmurray@sas.upenn.edu)

### Notes

The authors declare no competing financial interest.

## ■ ACKNOWLEDGMENTS

X.Y., J.F., T.P., and C.B.M. acknowledge support from the Office of Naval Research Multidisciplinary University Research Initiative on optical metamaterials through award N00014-10-1-0942. D.R.H. and B.T.D. are grateful for support from the U.S. Department of Energy Office of Basic Energy Sciences, Division of Materials Science and Engineering, under award no. DE-SC0002158. D.R.H. acknowledges additional support from the NSF-IGERT program (Grant DGE-0221664). B.T.D. acknowledges additional support from the IBM Ph.D. Fellowship Award. J.C. recognizes support from the Materials Research Science and Engineering Center program of the National Science Foundation (NSF) under award DMR-1120901. C.B.M. is also grateful to the Richard Perry University Professorship for support of his supervisor role. We thank Dr. Douglas Yates and Dr. Jamie Ford at the Penn Regional Nanotechnology Facility for support on electron microscopy, Dr. Paul Heiney for assistance with SAXS measurements, and Dr. David Vann for support with ICO-OES measurements.

## ■ REFERENCES

- (1) Costi, R.; Saunders, A. E.; Banin, U. *Angew. Chem., Int. Ed.* **2010**, *49*, 4878–4897.
- (2) Wang, C.; Tian, W.; Ding, Y.; Ma, Y.-Q.; Wang, Z. L.; Markovic, N. M.; Stamenkovic, V. R.; Daimon, H.; Sun, S. *J. Am. Chem. Soc.* **2010**, *132*, 6524–6529.
- (3) de Mello Donegá, C. *Chem. Soc. Rev.* **2011**, *40*, 1512–1546.
- (4) Carbone, L.; Cozzoli, P. D. *Nano Today* **2010**, *5*, 449–493.
- (5) Buck, M. R.; Schaak, R. E. *Angew. Chem., Int. Ed.* **2013**, *52*, 6154–6178.
- (6) Krylova, G.; Giovanetti, L. J.; Requejo, F. G.; Dimitrijevic, N. M.; Prakashenka, A.; Shevchenko, E. V. *J. Am. Chem. Soc.* **2012**, *134*, 4384–4392.
- (7) Read, C. G.; Biacchi, A. J.; Schaak, R. E. *Chem. Mater.* **2013**, *25*, 4304–4311.
- (8) Sun, Y.; Foley, J. J.; Peng, S.; Li, Z.; Gray, S. K. *Nano Lett.* **2013**, *13*, 3958–3964.
- (9) Buck, M. R.; Bondi, J. F.; Schaak, R. E. *Nat. Chem.* **2012**, *4*, 37–44.
- (10) Banin, U.; Ben-Shahar, Y.; Vinokurov, K. *Chem. Mater.* **2014**, *26*, 97–110.
- (11) Mokari, T.; Rothenberg, E.; Popov, I.; Costi, R.; Banin, U. *Science* **2004**, *304*, 1787–1790.
- (12) Mokari, T.; Sztrum, C. G.; Salant, A.; Rabani, E.; Banin, U. *Nat. Mater.* **2005**, *4*, 855–863.
- (13) Yang, J.; Elim, H. L.; Zhang, Q.; Lee, J. Y.; Ji, W. *J. Am. Chem. Soc.* **2006**, *128*, 11921–11926.
- (14) Motl, N. E.; Bondi, J. F.; Schaak, R. E. *Chem. Mater.* **2012**, *24*, 1552–1554.
- (15) Liang, S.; Liu, X.-L.; Yang, Y.-Z.; Wang, Y.-L.; Wang, J.-H.; Yang, Z.-J.; Wang, L.-B.; Jia, S.-F.; Yu, X.-F.; Zhou, L.; Wang, J.-B.; Zeng, J.; Wang, Q.-Q.; Zhang, Z. *Nano Lett.* **2012**, *12*, 5281–5286.
- (16) Guardia, P.; Korobchevskaya, K.; Casu, A.; Genovese, A.; Manna, L.; Comin, A. *ACS Nano* **2013**, *7*, 1045–1053.
- (17) Liu, X.; Lee, C.; Law, W.-C.; Zhu, D.; Liu, M.; Jeon, M.; Kim, J.; Prasad, P. N.; Kim, C.; Swihart, M. T. *Nano Lett.* **2013**, *13*, 4333–4339.
- (18) Wang, C.; Xu, C.; Zeng, H.; Sun, S. *Adv. Mater.* **2009**, *21*, 3045–3052.
- (19) Yu, H.; Chen, M.; Rice, P. M.; Wang, S. X.; White, R. L.; Sun, S. *Nano Lett.* **2005**, *5*, 379–382.
- (20) Shi, W.; Zeng, H.; Sahoo, Y.; Ohulchanskyy, T. Y.; Ding, Y.; Wang, Z. L.; Swihart, M.; Prasad, P. N. *Nano Lett.* **2006**, *6*, 875–881.
- (21) Wang, C.; Yin, H.; Dai, S.; Sun, S. *Chem. Mater.* **2010**, *22*, 3277–3282.
- (22) Wu, H.; Chen, O.; Zhuang, J.; Lynch, J.; LaMontagne, D.; Nagaoka, Y.; Cao, Y. C. *J. Am. Chem. Soc.* **2011**, *133*, 14327–14337.
- (23) Li, P.; Wei, Z.; Wu, T.; Peng, Q.; Li, Y. *J. Am. Chem. Soc.* **2011**, *133*, 5660–5665.
- (24) Seh, Z. W.; Liu, S.; Zhang, S.-Y.; Bharathi, M. S.; Ramanarayan, H.; Low, M.; Shah, K. W.; Zhang, Y.-W.; Han, M.-Y. *Angew. Chem., Int. Ed.* **2011**, *50*, 10140–10143.
- (25) Chen, Y.; Zeng, D.; Zhang, K.; Lu, A.; Wang, L.; Peng, D.-L. *Nanoscale* **2014**, *6*, 874–881.
- (26) Costi, R.; Saunders, A. E.; Elmalem, E.; Salant, A.; Banin, U. *Nano Lett.* **2008**, *8*, 637–641.
- (27) O'Connor, T.; Panov, M. S.; Mereshchenko, A.; Tarnovsky, A. N.; Lorek, R.; Perera, D.; Diederich, G.; Lambright, S.; Moroz, P.; Zamkov, M. *ACS Nano* **2012**, *6*, 8156–8165.
- (28) Acharya, K. P.; Khnayzer, R. S.; O'Connor, T.; Diederich, G.; Kirsanova, M.; Klinkova, A.; Roth, D.; Kinder, E.; Imboden, M.; Zamkov, M. *Nano Lett.* **2011**, *11*, 2919–2926.
- (29) Tahir, M. N.; Natalio, F.; Cambaz, M. A.; Panthöfer, M.; Branscheid, R.; Kolb, U.; Tremel, W. *Nanoscale* **2013**, *5*, 9944–9949.
- (30) Wang, C.; van der Vliet, D.; More, K. L.; Zaluzec, N. J.; Peng, S.; Sun, S.; Daimon, H.; Wang, G.; Greeley, J.; Pearson, J.; Paulikas, A. P.; Karapetrov, G.; Strmcnik, D.; Markovic, N. M.; Stamenkovic, V. R. *Nano Lett.* **2011**, *11*, 919–926.
- (31) Jiang, J.; Gu, H.; Shao, H.; Devlin, E.; Papaefthymiou, G. C.; Ying, J. Y. *Adv. Mater.* **2008**, *20*, 4403–4407.
- (32) Gao, J.; Liang, G.; Cheung, J. S.; Pan, Y.; Kuang, Y.; Zhao, F.; Zhang, B.; Zhang, X.; Wu, E. X.; Xu, B. *J. Am. Chem. Soc.* **2008**, *130*, 11828–11833.
- (33) Xu, C.; Xie, J.; Ho, D.; Wang, C.; Kohler, N.; Walsh, E. G.; Morgan, J. R.; Chin, Y. E.; Sun, S. *Angew. Chem., Int. Ed.* **2008**, *47*, 173–176.
- (34) Xu, C.; Wang, B.; Sun, S. *J. Am. Chem. Soc.* **2009**, *131*, 4216–4217.



- (35) Xie, J.; Zhang, F.; Aronova, M.; Zhu, L.; Lin, X.; Quan, Q.; Liu, G.; Zhang, G.; Choi, K.-Y.; Kim, K.; Sun, X.; Lee, S.; Sun, S.; Leapman, R.; Chen, X. *ACS Nano* **2011**, *5*, 3043–3051.
- (36) Figuerola, A.; Fiore, A.; Di Corato, R.; Falqui, A.; Giannini, C.; Micotti, E.; Lascialfari, A.; Corti, M.; Cingolani, R.; Pellegrino, T.; Cozzoli, P. D.; Manna, L. *J. Am. Chem. Soc.* **2008**, *130*, 1477–1487.
- (37) Pineider, F.; de Julián Fernández, C.; Videtta, V.; Carlino, E.; al Hourani, A.; Wilhelm, F.; Rogalev, A.; Cozzoli, P. D.; Ghigna, P.; Sangregorio, C. *ACS Nano* **2013**, *7*, 857–866.
- (38) Sheldon, M. T.; Trudeau, P.-E.; Mokari, T.; Wang, L.-W.; Alivisatos, A. P. *Nano Lett.* **2009**, *9*, 3676–3682.
- (39) Carbone, L.; Jakab, A.; Khalavka, Y.; Sönnichsen, C. *Nano Lett.* **2009**, *9*, 3710–3714.
- (40) Yang, J.; Ying, J. Y. *J. Am. Chem. Soc.* **2010**, *132*, 2114–2115.
- (41) Gu, H.; Zheng, R.; Zhang, X.; Xu, B. *J. Am. Chem. Soc.* **2004**, *126*, 5664–5665.
- (42) Teranishi, T.; Saruyama, M.; Nakaya, M.; Kanehara, M. *Angew. Chem., Int. Ed.* **2007**, *46*, 1713–1715.
- (43) Zhao, Y.; Pan, H.; Lou, Y.; Qiu, X.; Zhu, J.; Burda, C. *J. Am. Chem. Soc.* **2009**, *131*, 4253–4261.
- (44) Hsu, S.-W.; On, K.; Tao, A. R. *J. Am. Chem. Soc.* **2011**, *133*, 19072–19075.
- (45) Luther, J. M.; Jain, P. K.; Ewers, T.; Alivisatos, A. P. *Nat. Mater.* **2011**, *10*, 361–366.
- (46) Hessel, C. M.; P. Pattani, V.; Rasch, M.; Panthani, M. G.; Koo, B.; Tunnell, J. W.; Korgel, B. A. *Nano Lett.* **2011**, *11*, 2560–2566.
- (47) Kriegel, I.; Jiang, C.; Rodríguez-Fernández, J.; Schaller, R. D.; Talapin, D. V.; da Coma, E.; Feldmann, J. *J. Am. Chem. Soc.* **2012**, *134*, 1583–1590.
- (48) Xie, Y.; Riedinger, A.; Prato, M.; Casu, A.; Genovese, A.; Guardia, P.; Sottini, S.; Sangregorio, C.; Miszta, K.; Ghosh, S.; Pellegrino, T.; Manna, L. *J. Am. Chem. Soc.* **2013**, *135*, 17630–17637.
- (49) Palomaki, P. K. B.; Miller, E. M.; Neale, N. R. *J. Am. Chem. Soc.* **2013**, *135*, 14142–14150.
- (50) Manna, G.; Bose, R.; Pradhan, N. *Angew. Chem., Int. Ed.* **2013**, *52*, 6762–6766.
- (51) Kanehara, M.; Koike, H.; Yoshinaga, T.; Teranishi, T. *J. Am. Chem. Soc.* **2009**, *131*, 17736–17737.
- (52) Buonsanti, R.; Llordes, A.; Aloni, S.; Helms, B. A.; Milliron, D. J. *Nano Lett.* **2011**, *11*, 4706–4710.
- (53) Garcia, G.; Buonsanti, R.; Runnerstrom, E. L.; Mendelsberg, R. J.; Llordes, A.; Anders, A.; Richardson, T. J.; Milliron, D. J. *Nano Lett.* **2011**, *11*, 4415–4420.
- (54) Manthiram, K.; Alivisatos, A. P. *J. Am. Chem. Soc.* **2012**, *134*, 3995–3998.
- (55) Llordes, A.; Garcia, G.; Gazquez, J.; Milliron, D. J. *Nature* **2013**, *500*, 323–326.
- (56) Gordon, T. R.; Paik, T.; Klein, D. R.; Naik, G. V.; Caglayan, H.; Boltasheva, A.; Murray, C. B. *Nano Lett.* **2013**, *13*, 2857–2863.
- (57) Lee, J.; Lee, S.; Li, G.; Petruska, M. A.; Paine, D. C.; Sun, S. J. *Am. Chem. Soc.* **2012**, *134*, 13410–13414.
- (58) Della Gaspera, E.; Bersani, M.; Cittadini, M.; Guglielmi, M.; Pagani, D.; Noriega, R.; Mehra, S.; Salleo, A.; Martucci, A. *J. Am. Chem. Soc.* **2013**, *135*, 3439–3448.
- (59) Ye, X.; Chen, J.; Murray, C. B. *J. Am. Chem. Soc.* **2011**, *133*, 2613–2620.
- (60) Ye, X.; Chen, J.; Diroll, B. T.; Murray, C. B. *Nano Lett.* **2013**, *13*, 1291–1297.
- (61) Kang, Y.; Ye, X.; Murray, C. *Angew. Chem., Int. Ed.* **2010**, *49*, 6156–6159.
- (62) Wang, C.; Daimon, H.; Onodera, T.; Koda, T.; Sun, S. *Angew. Chem., Int. Ed.* **2008**, *47*, 3588–3591.
- (63) Kovalenko, M. V.; Bodnarchuk, M. I.; Talapin, D. V. *J. Am. Chem. Soc.* **2010**, *132*, 15124–15126.
- (64) Choi, D.-H.; Jeong, G.-H.; Kim, S.-W. *Bull. Korean Chem. Soc.* **2011**, *32*, 3851–3852.
- (65) Ye, X.; Jin, L.; Caglayan, H.; Chen, J.; Xing, G.; Zheng, C.; Doan-Nguyen, V.; Kang, Y.; Engheta, N.; Kagan, C. R.; Murray, C. B. *ACS Nano* **2012**, *6*, 2804–2817.
- (66) Ye, X.; Zheng, C.; Chen, J.; Gao, Y.; Murray, C. B. *Nano Lett.* **2013**, *13*, 765–771.
- (67) Burstein, E. *Phys. Rev.* **1954**, *93*, 632–633.
- (68) Williams, D. B.; Carter, C. B. *Transmission Electron Microscopy: A Textbook for Materials Science*; Plenum: New York, 1996.
- (69) Burbano, M.; Scanlon, D. O.; Watson, G. W. *J. Am. Chem. Soc.* **2011**, *133*, 15065–15072.
- (70) Shi, W.; Sahoo, Y.; Zeng, H.; Ding, Y.; Swihart, M. T.; Prasad, P. N. *Adv. Mater.* **2006**, *18*, 1889–1894.
- (71) Casula, M. F.; Jun, Y.-W.; Zaziski, D. J.; Chan, E. M.; Corrias, A.; Alivisatos, A. P. *J. Am. Chem. Soc.* **2006**, *128*, 1675–1682.
- (72) Kloper, V.; Osovsky, R.; Kolny-Olesiak, J.; Sashchiuk, A.; Lifshitz, E. *J. Phys. Chem. C* **2007**, *111*, 10336–10341.
- (73) Vazquez, Y.; Henkes, A. E.; Chris Bauer, J.; Schaak, R. E. *J. Solid State Chem.* **2008**, *181*, 1509–1523.
- (74) Moon, G. D.; Ko, S.; Min, Y.; Zeng, J.; Xia, Y.; Jeong, U. *Nano Today* **2011**, *6*, 186–203.
- (75) Son, D. H.; Hughes, S. M.; Yin, Y.; Paul Alivisatos, A. *Science* **2004**, *306*, 1009–1012.
- (76) Robinson, R. D.; Sadtler, B.; Demchenko, D. O.; Erdonmez, C. K.; Wang, L.-W.; Alivisatos, A. P. *Science* **2007**, *317*, 355–358.
- (77) Pietryga, J. M.; Werder, D. J.; Williams, D. J.; Casson, J. L.; Schaller, R. D.; Klimov, V. I.; Hollingsworth, J. A. *J. Am. Chem. Soc.* **2008**, *130*, 4879–4885.
- (78) Dawood, F.; Schaak, R. E. *J. Am. Chem. Soc.* **2009**, *131*, 424–425.
- (79) Cabot, A.; Smith, R. K.; Yin, Y.; Zheng, H.; Reinhard, B. M.; Liu, H.; Alivisatos, A. P. *ACS Nano* **2008**, *2*, 1452–1458.
- (80) Park, J.; Zheng, H.; Jun, Y.-W.; Alivisatos, A. P. *J. Am. Chem. Soc.* **2009**, *131*, 13943–13945.
- (81) Li, H.; Zanella, M.; Genovese, A.; Povia, M.; Falqui, A.; Giannini, C.; Manna, L. *Nano Lett.* **2011**, *11*, 4964–4970.
- (82) Saruyama, M.; So, Y.-G.; Kimoto, K.; Taguchi, S.; Kanemitsu, Y.; Teranishi, T. *J. Am. Chem. Soc.* **2011**, *133*, 17598–17601.
- (83) González, E.; Arbiol, J.; Puntès, V. F. *Science* **2011**, *334*, 1377–1380.
- (84) Zhang, H.; Solomon, L. V.; Ha, D.-H.; Honrao, S.; Hennig, R. G.; Robinson, R. D. *Dalton Trans.* **2013**, *42*, 12596–12599.
- (85) Zhang, H.; Hyun, B.-R.; Wise, F. W.; Robinson, R. D. *Nano Lett.* **2012**, *12*, 5856–5860.
- (86) Khon, E.; Mereshchenko, A.; Tarnovsky, A. N.; Acharya, K.; Klinkova, A.; Hewa-Kasakarage, N. N.; Nemitz, I.; Zamkov, M. *Nano Lett.* **2011**, *11*, 1792–1799.
- (87) Yin, Y.; Rioux, R. M.; Erdonmez, C. K.; Hughes, S.; Somorjai, G. A.; Alivisatos, A. P. *Science* **2004**, *304*, 711–714.